Real-Time Frequency Characterization of Chirped Lasers via Finite-Difference Phase Measurements

Xuebing Zhang, *Member, IEEE*, Javier Pérez Santacruz, Jac Romme, Amir Abbas Kashi, Qianhao Lin, Gijs van Elzakker, Marcus Dahlem, Dongjae Shin, *Senior Member, IEEE*, and Ruud Oldenbeuving, *Member, IEEE*

***Abstract*—Laser instantaneous frequency (LIF) describes the time-varying frequency of a laser signal, defined as the temporal derivative of the oscillation phase divided by 2π. This concept is crucial in understanding frequency noise, phase noise, and chirped optical signals, where the frequency changes over time. Most current optical frequency measurements rely on frequency-domain analysis, which face limitations when applied to rapidly chirped lasers. Unlike frequency-domain methods, time-domain methods provide a more accurate representation of the time-varying frequency of chirped lasers, which is crucial for real-time applications. The widely used Hilbert transform-based method describes the LIF measurement but has slow real-time responses, a relatively low measurement speed, a not on-chip-compatible structure, and the ambiguity of the chirp sign, which hampers its use, particularly in real-time applications. This paper introduces a novel real-time LIF estimator for chirped lasers, offering higher accuracy, reduced algorithm complexity, and an on-chip integration solution. Experimental demonstrations include applications for FMCW LiDAR adaptive nonlinearity correction and real-time photoelectric control loops.**

***Index Terms*—Chirped laser, FMCW LiDAR, laser instantaneous frequency (LIF) estimation, photonic integrated circuits, real-time.**

I. Introduction

FAST linear frequency-modulated continuous-wave (FMCW) lasers are gaining significant attention in various applications such as distance, velocity, and vibration measurements [1], [2], light detection and ranging (LiDAR) [3], and optical coherence tomography (OCT) [4], [5]. Compared to external modulation-based linear frequency chirp (e.g., a single-sideband modulation), direct frequency chirp of a laser has simpler electrical and optical structures. It also does not require high-speed and expensive electrical generators and amplifiers such as an arbitrary waveform generator (AWG)

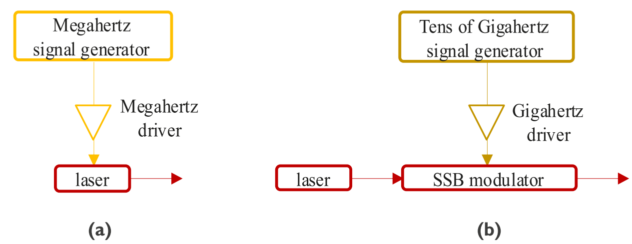

Fig. 1. Fast optical frequency chirp generations, (a) direct laser driven-based; (b) external frequency modulation-based. SSB: single-side band.

and a gigahertz-level driver to achieve a gigahertz-level chirp range as shown in Fig. 1 [6]. However, direct driving introduces chirp nonlinearity and frequency instability, which reduce system performance [7]. To address these challenges, digital predistortion techniques are proposed to correct distortions caused by nonlinearities in the system [7], [8]. However, these methods rely heavily on ultra-accurate laser instantaneous frequency (LIF) measurements, which are essential for characterizing the instantaneous behavior of the laser frequency and phase change.

LIF refers to the time-dependent frequency of a laser signal. It is defined as the temporal derivative of the oscillation phase divided by 2π. This concept is particularly important in the context of frequency/phase noise and chirping signals, where the frequency changes quickly over time. Currently, a delayed self-heterodyne interferometer-based structure is widely used to estimate the optical instantaneous frequency of a fast chirped laser enabled by Hilbert transform [7], [8], [9]. Hilbert transform converts the signal from the real plane into the complex plane, and the phase is extracted to estimate the instantaneous optical frequency. This transformation, however, has limitations, such as ambiguity in distinguishing the sign of $\pm$chirp, reduced accuracy for low beat frequencies, and relatively low real-time responses. The $\pm$chirp ambiguity arises from the loss of chirp sign information during the optical-to-electrical (O-E) conversion in the real domain, where negative frequencies are not represented [10]. By using a long optical delay line, typically up to several meters, a low beat frequency can be avoided [7]. However, such a large structure potentially prohibits on-chip integration, which is essential for more compact and stable photonic integrated circuits (PIC) solutions in the future [1], [11]. Additionally, the relatively low update rate of frame-by-frame signal processing is unsuitable for real-time scenarios [12], [13].

Received 1 August 2025; revised 21 January 2026 and 24 February 2026; accepted 1 March 2026. Date of publication 4 March 2026; date of current version 16 May 2026. This work was supported by the PhotonDelta National Grow Fund Programme - www.photondelta.com. *(Corresponding author: Xuebing Zhang.)*

Xuebing Zhang, Javier Pérez Santacruz, Jac Romme, Amir Abbas Kashi, Qianhao Lin, Gijs van Elzakker, Dongjae Shin, and Ruud Oldenbeuving are with IMEC-NL Holst Centre, 5656 AE Eindhoven, The Netherlands (e-mail: xuebing.zhang@imec.nl; javier.perezsantacruz@imec.be).

Marcus Dahlem is with the IMEC, 3001 Leuven, Belgium.

Color versions of one or more figures in this article are available at https://doi.org/10.1109/JLT.2026.3670732.

Digital Object Identifier 10.1109/JLT.2026.3670732

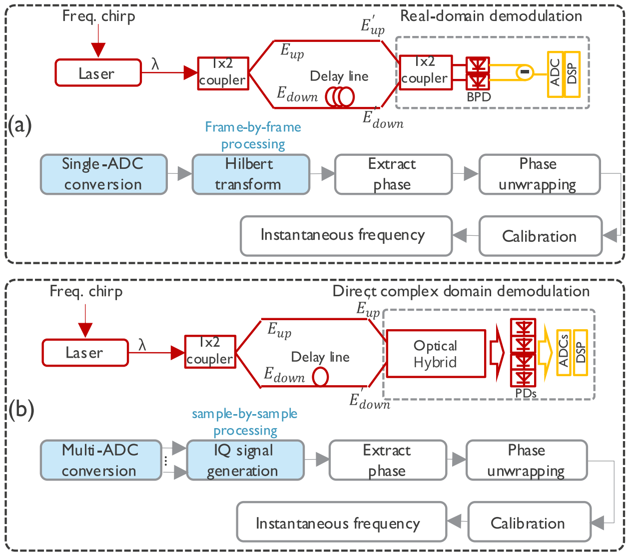

Fig. 2. Angle diversity-based direct complex-domain OPFD.

In our previous work [14], the concept was first proposed. In this paper a more completed theoretical analysis and the detailed structures are investigated. The novel real-time optical instantaneous frequency estimation method surpasses the Hilbert transform-based approach in accuracy. It uses an angle-diversity optical delayed self-heterodyne structure for direct complex-domain digital signal processing (DSP), eliminating $\pm$chirp ambiguity and substantial errors in low-beat-frequency cases. This method allows for shorter delay lines, enabling more compact on-chip integration, and reduces algorithm complexity, shortening DSP-caused delays. The sample-by-sample instantaneous frequency tracking supports real-time applications like fast feedback control loops [14].

This manuscript is organized as follows: Section II studies and analyses the principles, the angle-diversity structures, and the related DSP of the proposed direct complex domain LIF estimation method; Section III presents the simulation results using the proposed 3-angle diversity architecture and compares with the Hilbert transform-based estimation; Section IV introduces several applications in FMCW chirp linearization, FMCW LiDAR phase noise compensation, real-time laser wavelength locking; lastly, Section V concludes with the key points of this work.

II. Principles

A. Direct Complex-Domain Optical Phase Finite Difference

Fig. 2(a) presents the traditional laser chirp measurement approach, which is based on a delayed self-heterodyne interferometer using an optical balanced detection [8]. For a fast chirped laser, the non-delayed laser frequency will be different from the frequency after delay ($Freq_{E'_{up}} \neq Freq_{E'_{down}}$). As a result, the beat signal detected by the balanced photodiode (BPD) is a radiofrequency (RF) signal in real domain. And the instantaneous frequency of the laser can be described by the phase item of the beat RF signal. The phase information is extracted by using Hilbert transform in the digital domain [8]. The frequency nonlinearity is measured by acquiring a complete chirp signal. As noted in Section I, challenges in distinguishing the chirp's sign, the reduced accuracy for low beat frequencies, and the low real-time responses remain unresolved. When the laser frequencies with and without the delay line are equal ($Freq_{E'_{up}} = Freq_{E'_{down}}$), the widely-used frequency domain analysis (it is based on optical interference.) can be effectively used to measure optical frequency. However, it is not an instantaneous frequency and thus it is not suitable for fast and continuously chirped lasers [15], [16].

To solve these problems, we propose a novel direct complex-domain (DCD) optical phase finite difference (OPFD) method to real-time estimate ILF as shown in Fig. 2(b). This is a time-domain analyzing method supporting both $Freq_{E'_{up}} = Freq_{E'_{down}}$ and $Freq_{E'_{up}} \neq Freq_{E'_{down}}$ scenarios. Compared to the Hilbert transform-based method, the proposed approach uses angle-diversity beat signals to directly process signal in complex domain without using complex Hilbert transform. Consequently, phase extraction can be performed on a sample-by-sample basis rather than a frame-by-frame basis. Firstly, this procedure eliminates the $\pm$chirp ambiguity due to the unrecognized $\pm$beat-frequency. It then enhances the real-time response performance. Additionally, the previously required long delay time/line (meter-level) from Hilbert transform in Fig. 2(a), can be significantly reduced without compromising accuracy, facilitating easier system integration. The proposed method employs a delayed self-heterodyne interferometer structure with angle-diversity detection. An FMCW laser is initially divided into two paths using a 1-by-2 coupler. The upper path signal, referred to as signal-up ($E_{up}(t)$), is directly sent to an optical hybrid, which generates multiple outputs of identical intensity but with different phase shifts for each input port [17], [18]. Meanwhile the lower path passes through a delay-line and finally combine with $E'_{up}(t)$ in the optical hybrid. We set it as signal-down ($E'_{down}(t)$), then the signals can be presented as

$$E\left(t\right) = A_{FMCW}\left(t\right) \cdot \cos\left[\phi_{FMCW}\left(t\right)\right], \tag{1}$$

$$E'_{up}\left(t\right) = A'_{FMCW}\left(t\right) \cdot \sqrt{2}\big/_{2} \cos\left[\phi_{FMCW}\left(t\right)\right], \tag{2}$$

$$E'_{down}\left(t\right) = A'_{FMCW}\left(t-\tau\right) \cdot \sqrt{2}\big/_{2} \cos\left[\phi_{FMCW}\left(t-\tau\right)\right], \tag{3}$$

$E(t)$ is the electric field of the FMCW light with unit amplitude. $\phi_{FMCW}(t)$ is the phase of the chirped laser. And $A_{FMCW}(t)$ is the additional intensity modulation accompanying frequency chirp. As the arm power imbalance can be eliminated by using the method in Fig. 5(b), to make analysis simpler, $A'_{FMCW}(t)$ and $A'_{FMCW}(t-\tau)$ are used to represent the amplitudes of optical Hybrid input signals after correcting the delay line loss-caused inter-arm power imbalance. Here, $A'_{FMCW}(t) = \alpha_{loss} \cdot A_{FMCW}(t), \alpha_{loss} < 1$. The laser angular frequency can be liner or nonlinear. τ is the waveguide time delay in the delayed path.

The optical hybrid combines $E'_{up}(t)$ and $E'_{down}(t)$ into several sub-groups. Each of them will be detected by a photodiode

(PD) [18]. All detected photocurrents have equal amplitude with uniformly increased phase shifting. They are then sampled by analog-to-digital converters (ADCs) and analyzed in digital domain. Considering the PD responsivity of R_{pd}, the photocurrents can be expressed as

$$I_k(t) = \frac{R_{pd}}{2N} \times \left| \begin{array}{c} A'_{FMCW}(t) \cdot cos\left[\phi_{FMCW}(t)\right] \\ +A'_{FMCW}(t-\tau) \cdot cos\left[\phi_{FMCW}(t-\tau) + \varphi_k\right] \end{array} \right|^2, \tag{4}$$

Since a PD is a low pass filter, the high frequency beat notes are out of the PD bandwidth. Thus, the calculated photocurrents could be simplified as, (5) shown at the bottom of this page,

$$\varphi_k = (k-1) \cdot \frac{2\pi}{N}, \tag{6}$$

$I_k(t)$ is the k^{th} detected photocurrent. N is the number of diverse angles (N is also the number of output ports). φ_k is the phase shift in each sub-group generated by the optical hybrid. The optical phase difference is transferred from optical domain to electrical domain (in beat note). To extract the phase component of the beat signal, the real signal must be transformed into the complex domain. This transformation is achieved by defining a new calculation using angle diversity beat notes. Consequently, the complex domain signal ($IQ(t)$) can be recovered as

$$IQ(t) = \sum_{k=1}^{N} \left[I_k(t) \times e^{j\varphi_k}\right], \tag{7}$$

From Euler's Formula [19], a cosine signal can be written as

$$\cos(\theta) = \frac{e^{j\theta} + e^{-j\theta}}{2}, \tag{8}$$

Substitute (5), (6), and (8) into (7), the $IQ(t)$ can be rewritten as

$$IQ(t) = R_A(t) \cdot \frac{R_{pd}}{2N} \sum_{k=1}^{N} \left[e^{j\varphi_k} + \frac{1}{2} e^{j\Delta\varphi_{FMCW}} + \frac{1}{2} e^{-j(\Delta\varphi_{FMCW} - 2\varphi_k)} \right], \tag{9}$$

$$R_A(t) = A'_{FMCW}(t) \cdot A'_{FMCW}(t-\tau), \tag{10}$$

Here, $\Delta\varphi_{FMCW}$ is $\phi_{FMCW}(t) - \phi_{FMCW}(t-\tau)$. As $\sum_{k=1}^{N}(\varphi_k) = 2\pi$, we can get $\sum_{k=1}^{N}(e^{j\varphi_k}) = 0$, and $\sum_{k=1}^{N}(e^{-j(\Delta\varphi_{FMCW} - 2\varphi_k)}) = 0$. Then (9) can be presented as

$$IQ(t) = R_A(t) \cdot \frac{R_{pd}}{4} \times e^{j[\phi_{FMCW}(t) - \phi_{FMCW}(t-\tau)]}, \tag{11}$$

Each photocurrent is multiplied by a matched phase item (in (7)), which is generated through the optical hybrid, and the results are accumulated. This process ultimately yields a complex signal using OPFD method. Then the phase of the beat signal can be easily extracted

$$\begin{aligned} \phi_{beat}(t) &= \phi_{FMCW}(t) - \phi_{FMCW}(t-\tau) \\ &= \frac{d\phi_{FMCW}(t)}{2\pi dt} \cdot 2\pi\tau. \end{aligned} \tag{12}$$

when $1/\tau$ is much larger than laser frequency chirping speed, $\frac{d\phi_{FMCW}(t)}{2\pi dt}$ can be used to accurately estimate the instantaneous frequency of the chirped laser. The delay selection depends on the chirping speed. Typically, a faster frequency change needs a shorter time delay. On the other hand, τ matters the sensitivity of the frequency/phase change. A longer delay can enhance this sensing ability. Therefore, τ needs to be optimized in different applications. Using multiple PD outputs together with straightforward calculations makes it possible to extract the phase component of the beat signal without relying on a complex Hilbert transform, thereby eliminating the distortions that the Hilbert transform can introduce. Additionally, as the beat phase is extracted sample-by-sample, the laser's instantaneous frequency is also estimated sample-by-sample. This method is faster than Hilbert transform-based approach. The DSP is working in complex domain directly, there is no ±chirp ambiguity, meaning more accurate. By extracting the phase term in (12), this method eliminates the estimation accuracy loss caused by chirp-induced intensity deviations in traditional approaches. As a result, it becomes immune to laser intensity fluctuations.

B. Angle Diversity Architectures and Digital Signal Processing

In this section, three types of angle diversity structures are proposed and analyzed. The first type is the 4-angle diversity detecting structure, commonly known as the optical coherent receiver [18]. Fig. 3(a) illustrates the 4-angle diversity DCD OPFD design using an optical 90° hybrid. By substituting its angle shifts into (5), four photocurrents can be obtained as below (13)–(16) shown at the bottom of the next page, $I_1(t), I_2(t), I_3(t), I_4(t)$ are the detected photocurrents (real values). The recovered complex signal from (9) is described as

$$\begin{aligned} IQ_{4-angle}(t) &= I_1(t) + I_2(t) \times \mathrm{e}^{\frac{j\pi}{2}} + I_3(t) \times \mathrm{e}^{j\pi} + I_4(t) \times \mathrm{e}^{\frac{j3\pi}{2}} \\ &= R_A(t) \cdot \frac{R_{pd}}{4} \mathrm{e}^{j[\phi_{FMCW}(t) - \phi_{FMCW}(t-\tau)]}, \end{aligned} \tag{17}$$

Then the phase of the beat signal can be extracted using angle calculations.

When changing the relative angle shift among optical hybrid outputs from 90° to 120°, the 3-angle diversity DCD OPFD design can be achieved [17] as shown in Fig. 3(b). Then similar

$$I_k(t) = \frac{R_{pd}}{2N} \left\{ \begin{array}{c} \frac{1}{2}\left[\left|A'_{FMCW}(t)\right|^2 + \left|A'_{FMCW}(t-\tau)\right|^2\right] + A'_{FMCW}(t) \\ \cdot A'_{FMCW}(t-\tau) \cdot \cos\left[\phi_{FMCW}(t) - \phi_{FMCW}(t-\tau) - \varphi_k\right] \end{array} \right\}, \tag{5}$$

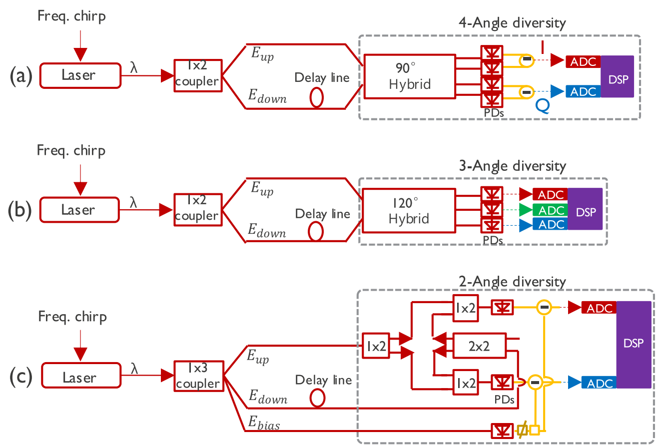

Fig. 3. Angle diversity-based direct complex-domain OPFD structures; (a) 4-angle, (b) 3-angle, (c) 2-angle diversity designs.

calculations are presented as

$$\begin{aligned} IQ_{3-angle}(t) &= I_1(t) + I_2(t) \times \mathrm{e}^{\frac{j2\pi}{3}} + I_3(t) \times \mathrm{e}^{\frac{j4\pi}{3}} \\ &= R_A(t) \cdot \frac{R_{pd}}{4} \mathrm{e}^{j[\phi_{FMCW}(t) - \phi_{FMCW}(t-\tau)]}, \end{aligned} \tag{18}$$

As analyzed above, it can be inferred that the angle-diversity structure is not limited to three or four angles. The number of diverse angles can be larger or smaller.

Typically, a larger port-count coupler is more challenging to design and fabricate, and it tends to have more phase errors. Additionally, structures with more outputs require more resources. As shown in Fig. 3(a), the 4-angle design uses four PDs and two ADCs. The reduction in number of ADCs (normally four) is achieved through analog subtraction calculations. In contrast, the 3-angle design uses fewer resources (three PDs and three ADCs) and is relatively easier to be implemented. In principle, a 2-angle diversity design will use even fewer resources, particularly fewer expensive ADCs. But the same design rules cannot be inherited from 4-/3-angle diversity structures directly. Because if we follow their design rules, the angle-set will be 0° and 180°, which could be recovered into the complex domain. Therefore, we propose a new 2-angle diversity structure using simpler and less-error optical couplers, three PDs, and two ADCs. In this approach, the angle set of 0° and 90° is utilized. The detailed analysis is depicted below. Fig. 3(c) presents the principle of the proposed structure, which consists of three 1-by-2 couplers, a 2-by-2 coupler, a 1-by-3 coupler, and two PDs. Laser light is first fed into the 1-by-3 coupler, which splits the light into three paths: up, down, and bias paths. The upper path beam $E_{up}(t)$ is further split into two beams with identical intensity and phase. The lower path beam $E_{down}(t)$ passes through a long delay line and a 2-by-2 coupler.

By using the 2-by-2 coupler, two beams with the same intensity but a 90° phase shift are created and are then separately merged with the two beams generated in the upper path via additional two 2-by-1 couplers. The outputs of two 2-by-1 couplers are detected by two PDs, each producing an asymmetrical Mach-Zehnder interferometer (MZI) response. Thus, a pair of MZIs with 90° phase shifting is achieved. According to (5), two photocurrents can be written as (19)–(20) shown at the bottom of the next page. However, if apply the same calculation in (8), the extracted phase will remain in the first quadrant, which is not able to cover the entire complex plane as shown in Fig. 4(c) before the unipolar-to-bipolar conversion. Vectors $I_k(t) \times e^{j\varphi_k}$ can cover the entire complex plane using either four or three angles, as illustrated in the first two scenarios in Fig. 4(a)–(b). To solve the problem, we propose a unipolar-to-bipolar conversion method when $A'_{FMCW}(t) \approx A'_{FMCW}(t-\tau)$. This means the laser amplitude maintains after the very short time delay of τ (e.g., 1–10 ns). For many applications, this condition is easy to meet [8], [14]. Then simplified $I_1(t)$ and $I_2(t)$ are $I_1(t) = R_{pd} \cdot |A'_{FMCW}(t)|^2/12 \cdot \{1 + \cos[\phi_{FMCW}(t) - \phi_{FMCW}(t-\tau)]\}$ and $I_2(t) = R_{pd} \cdot |A'_{FMCW}(t)|^2/12 \cdot \{1 + \cos[\phi_{FMCW}(t) - \phi_{FMCW}(t-\tau) - \frac{\pi}{2}]\}$. A third path ($I_3(t)$) is utilized to supply the bias current in the electrical domain after O-E conversion. $I_3(t) = R_{pd} \cdot |A'_{FMCW}(t)|^2/6$. An electrical attenuator and power splitter are employed to provide correct bias currents. $I_1(t)$and $I_2(t)$ will separately exclude this bias current to convert into bipolar signals as presented in Fig. 3(c). Consequently, the complex signal can be expressed as

$$\begin{aligned} IQ_{2-angle}(t) = {} & [I_1(t) - I_{bias}(t)] + [I_2(t) - I_{bias}(t)] \\ & \times \mathrm{e}^{\frac{j\pi}{2}}, \end{aligned} \tag{21}$$

$$I_1(t) = \frac{R_{pd}}{8} \left\{ \begin{array}{l} \frac{1}{2}\left[|A'_{FMCW}(t)|^2 + |A'_{FMCW}(t-\tau)|^2 \right] + A'_{FMCW}(t) \\ \cdot A'_{FMCW}(t-\tau) \cdot \cos[\phi_{FMCW}(t) - \phi_{FMCW}(t-\tau)] \end{array} \right\}, \tag{13}$$

$$I_2(t) = \frac{R_{pd}}{8} \left\{ \begin{array}{l} \frac{1}{2}\left[|A'_{FMCW}(t)|^2 + |A'_{FMCW}(t-\tau)|^2 \right] + A'_{FMCW}(t) \\ \cdot A'_{FMCW}(t-\tau) \cdot \cos\left[\phi_{FMCW}(t) - \phi_{FMCW}(t-\tau) - \frac{\pi}{2}\right] \end{array} \right\}, \tag{14}$$

$$I_3(t) = \frac{R_{pd}}{8} \left\{ \begin{array}{l} \frac{1}{2}\left[|A'_{FMCW}(t)|^2 + |A'_{FMCW}(t-\tau)|^2 \right] + A'_{FMCW}(t) \\ \cdot A'_{FMCW}(t-\tau) \cdot \cos[\phi_{FMCW}(t) - \phi_{FMCW}(t-\tau) - \pi] \end{array} \right\}, \tag{15}$$

$$I_4(t) = \frac{R_{pd}}{8} \left\{ \begin{array}{l} \frac{1}{2}\left[|A'_{FMCW}(t)|^2 + |A'_{FMCW}(t-\tau)|^2 \right] + A'_{FMCW}(t) \\ \cdot A'_{FMCW}(t-\tau) \cdot \cos\left[\phi_{FMCW}(t) - \phi_{FMCW}(t-\tau) - \frac{3\pi}{2}\right] \end{array} \right\}, \tag{16}$$

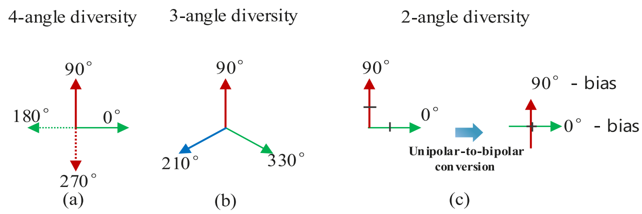

Fig. 4. IQ signal recovery in complex plane.

By adjusting the electrical attenuator, the bias current can be set to the correct level:

$$I_{bias}(t) = \frac{1}{2}\max\left(I_1(t)\right) = \frac{R_{pd}\cdot\left|A'_{FMCW}(t)\right|^2}{12}, \quad (22)$$

Then the final IQ signal can be obtained by substituting simplified $I_1(t)$, $I_2(t)$ and (22) into (21).

$$IQ_{2-angle}(t) = \frac{R_{pd}\cdot\left|A'_{FMCW}(t)\right|^2}{12} \times e^{j[\phi_{FMCW}(t)-\phi_{FMCW}(t-\tau)]}. \quad (23)$$

A calibration procedure is necessary to find the appropriate bias current. A feasible approach is to inject an amplitude-maintained triangle-chirp signal and obtain the sinusoidal photocurrent at the 0° output port and the cosine photocurrent response at 90° output port. Then tune the attenuator until the DC component is totally removed.

C. System Integration

This section will discuss the considerations for system integration. To optimize a photoelectric system, a fully integrated structure is crucial for minimizing size and enhancing system stability. The proposed structures leverage current integrated silicon photonics, which offer nearly all required building blocks.

Firstly, key optical hybrids can be realized using multimode interferometers (MMIs). For instance, a 4-by-4 MMI can function as a 90° hybrid, while a 3-by-3 MMI can serve as a 120° hybrid [17]. Other optical couplers can also be replaced by corresponding 1-by-2/2-by-2/1-by-3 MMIs. Secondly, current Ge PDs on the silicon photonic platform can be above 50 GHz, which easily supports high-speed applications [20]. ADCs, Transimpedance amplifiers (TIAs), and DSP technologies already have mature solutions in high-speed optical communications [21]. It is important to note that the bandwidth requirement is relatively low (e.g., ~100-MHz level for PDs). Additionally, bandwidth can be further reduced by minimizing time delay and/or decreasing chirp range/speed.

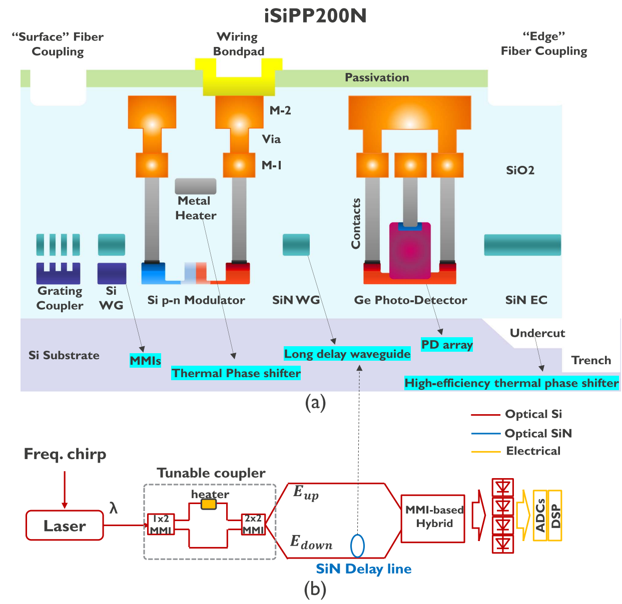

Fig. 5. (a) IMEC iSiPP200 Si-SiN platform, (b) The integrated photonic system on iSiPP200 Si-SiN platform.

The most challenging part for system integration comes from the long delay line/waveguide. In the proposed approach, the delay line has been significantly minimized (as shown in Section IV (a)). However, the tradeoff between time delay and signal detecting sensitivity, as described in (8), indicates that the delay line cannot be reduced indefinitely. On the other hand, extending the length of delay waveguides will lead to higher propagation loss, potentially compromising the design. For instance, the propagation loss of the silicon single mode waveguide in IMEC iSiPP50G platform is ~2 dB/cm. If the delay line is one-meter-level (used in traditional methods) [8], [22], [23], the total loss is roughly 200 dB, which is not acceptable. Even if the length is reduced to 20 cm (5x lower), the loss is around 40 dB (still not acceptable). Therefore, a low loss waveguide is essential for an integrated DCD OPFD structure. IMEC iSiPP200 platform offers both silicon photonic devices including silicon MMIs, high-speed PDs, and ultra-low loss (~0.2 dB/cm) SiN waveguides, which offers a promising solution as shown in Fig. 5(a) [24]. If we re-calculate, the loss of the delay line will be 4-dB level for a 20-cm waveguide, which is acceptable. To address the power imbalance between $E_{up}(t)$ and $E_{down}(t)$, an enhanced design is proposed in Fig. 5(b). The laser signal is first fed into an optical tunable coupler based on a symmetric MZI structure using 1-by-2/2-by-2 MMIs and a heater-based phase shifter (A high-efficiency thermal phase shifter can also be realized by using the provided Undercut

$$I_1(t) = \frac{R_{pd}}{12}\left\{\begin{matrix}\frac{1}{2}\left[\left|A'_{FMCW}(t)\right|^2 + \left|A'_{FMCW}(t-\tau)\right|^2\right] + A'_{FMCW}(t) \\ \cdot A'_{FMCW}(t-\tau)\cdot\cos\left[\phi_{FMCW}(t) - \phi_{FMCW}(t-\tau)\right]\end{matrix}\right\}, \quad (19)$$

$$I_2(t) = \frac{R_{pd}}{12}\left\{\begin{matrix}\frac{1}{2}\left[\left|A'_{FMCW}(t)\right|^2 + \left|A'_{FMCW}(t-\tau)\right|^2\right] + A'_{FMCW}(t) \\ \cdot A'_{FMCW}(t-\tau)\cdot\cos\left[\phi_{FMCW}(t) - \phi_{FMCW}(t-\tau) - \frac{\pi}{2}\right]\end{matrix}\right\}, \quad (20)$$

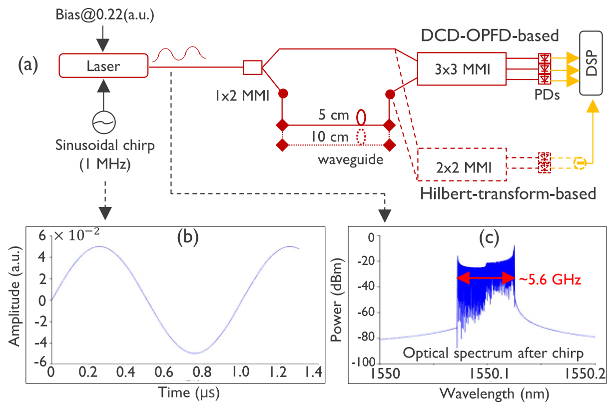

Fig. 6. Simulations in Lumerical, (a) schematic of the system, (b)-(c) sine-wave chirp and spectrum of the chirp.

technique.). It can split more optical power into the lossy delay path to balance power in two arms. For the long delay section, SiN waveguides will be utilized by transitioning light from Si to SiN and then back to Si waveguides. This approach can reduce propagation loss significantly. Silicon devices, such as MMI-based optical hybrids and PDs, can effectively support our angle-diversity detection structures.

III. Simulation Results

In this section, a system simulation of measuring a chirped laser's instantaneous frequency is described using Lumreical Interconnect and MATLAB. Fig. 6(a) illustrates the schematic of the simulation setup. A direct modulated laser (DML), driven by a sinusoidal signal, generates a sine-shaped frequency chirp that emulates nonlinear chirp behaver, incorporating both slow and fast chirp variations. The laser operates at a central wavelength of 1550 nm with an output power of 10 mW. The chirped laser signal is fed into a delayed self-heterodyne interferometer structure comprising a delay waveguide with a dimension of 450 nm $\times$ 220 nm. The waveguide has an effective index of 2.357 and a group index of 4.333, respectively. 5-cm and 10-cm waveguides are tested in the experiment to create time delays of 393.1 ps and 786.2 ps. As the power imbalance between two arms can be compensated by using the proposed structure in Fig. 5(b) and the waveguide loss can be significantly reduced by using low loss materials. For simplicity, the delay loss is assumed to be zero in the simulation. The 120° optical hybrid in angle-diversity detection is an optical 3-by-3 MMI followed by three PDs. Each PD has a bandwidth of only 62.5 MHz, a dark current of 15 nA, and a responsivity of 0.8 A/W. The sampled three photocurrents are processed digitally. The sinusoidal chirp signal is set as 1 MHz to minimize simulation time in Lumerical Interconnect as shown in Fig. 6(b). The chirp frequency range is ~5.6 GHz as presented in Fig. 6(c). The sampling rate is set as 64 GSa/s and simulation time is 1.3 μs. Key simulation parameters are summarized in Table I.

For simulation results, we first present the 3-by-3 MMI design and phase/intensity responses. Fig. 7(a) shows the design parameters of the 3-by-3MMI-based Silicon Hybrid. The silicon layer has a thickness of 220 nm. Its body size is 125 $\times$ 7.2 μm^2. Each side of the body section comprises three input/output tapers that transition the waveguide width from 0.45 μm at input to 2.1 μm at output over a length of 30 μm. The central taper is center-aligned with the body section and the vertical spacing between two tapers is 2.4 μm. Its simulated field profile is shown in Fig. 7(b). Results of phase and intensity responses at 1550 nm are illustrated in Table II. In this design, port In1 and In3 are selected as inputs. At outputs, the phase offsets that will be transferred into the electrical domain are $-119.85°$ (Phase_Out1_In1 - Phase_ Out1_In3), 0° (Phase_Out2_In1 - Phase_Out2_In3), and 119.85° (Phase_Out3_In1 - Phase_Out3_In3), respectively.

TABLE I
Key Simulation Parameters

Key parameters	Values
Sample rate	64 GSa/s
Simulation time	1.3 μs
Laser wavelength	1550 nm
Laser power	10 mW
Laser type	DML
Waveguide effective index $n_{eff,TE}$	2.357@1550 nm
Waveguide group index $n_{g,TE}$	4.333@1550 nm
Waveguide length difference	5 cm/10 cm
Delay time	393.1 ps/786.2 ps
PD responsivity	0.8 A/W
PD dark current	15 nA
PD bandwidth	62.5 MHz

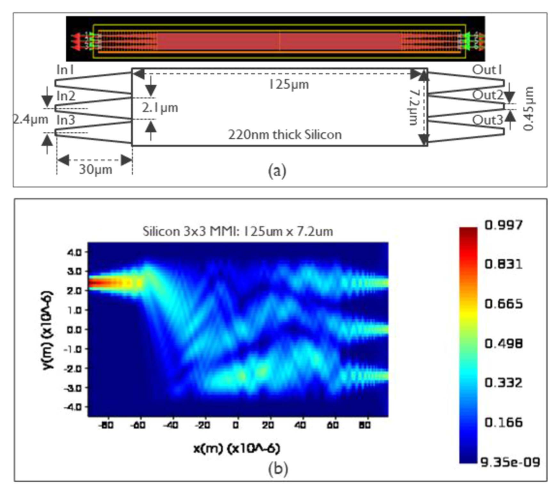

Fig. 7. 3-by-3 MMI simulation in Lumerical, (a) 3-by-3MMI parameters, (b) field profile in Lumerical MODE simulation.

TABLE II
Transmission Matrix-Phase (°) and Normalized Power (a.u.)

Port	Out1	Out2	Out3
In1	41.63° (PWR=0.3035)	-136.33° (PWR=0.2907)	161.48° (PWR=0.2786)
In2	-136.33° (PWR=0.2907)	161.54° (PWR=0.2563)	-136.33° (PWR=0.2907)
In3	161.48° (PWR=0.2786)	-136.33° (PWR=0.2907)	41.63° (PWR=0.3035)
φ_k:k=1,2,3	φ_1: -119.85°	φ_2: 0°	φ_3: 119.85°

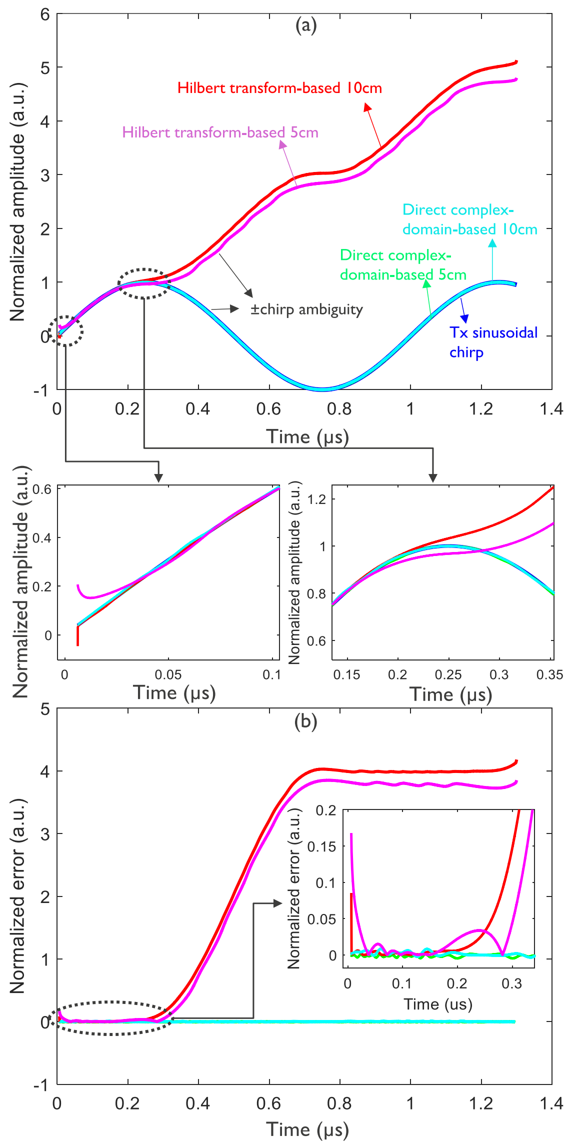

Fig. 8. Simulation results, (a) normalized amplitude responses, (b) normalized errors.

And the maximum power (PWR) imbalance among three optical output ports is 0.372 dB.

Fig. 8(a) and (b) compare the performance of the proposed DCD OPFD-based approach with the Hilbert transform-based method. The estimated frequency chirps from both methods are evaluated against the transmitted (Tx) chirp signal (shown in Fig. 8(b)) by fitting the Tx sine-wave chirp to the recovered curves and normalizing it to unit amplitude. The simulation results reveal that the Hilbert transform-based scheme suffers from the ±chirp ambiguity, where the estimated frequency consistently shifts towards one direction. This limitation prevents accurate tracking of common chirp profiles such as a sinusoidal chirp or a triangular chirp commonly used in a FMCW LiDAR system. Furthermore, the estimation accuracy of the Hilbert method decreases when the delay waveguide length is reduced from 10 cm to 5 cm. This degradation is primarily due to the shorter time-window (the sampling sequence length), which reduces the accuracy of Hilbert transform signal processing. At a fixed chirp speed of 1 MHz, a shorter delay line lowers the beating frequency, requiring a longer processing sequence to achieve sufficient high spectral resolution for Hilbert transformation. As shown in the insects of Fig. 8(a), Hilbert transformation-based approach exhibits larger estimation errors at the beginning of the chirp and in low-speed chirp regions. Moreover, the estimation errors are enlarged with a shorter delay line.

TABLE III
COMPARISON BETWEEN HILBERT TRANSFORM-BASED AND DIRECT COMPLEX-DOMAIN-BASED METHODS

Calculating time zone	Relative errors	Hilbert transform-based	Direct complex domain-based
0 - 0.25 μs	Error_pp@ 10 cm	0.0853	0.0062
0 - 0.25 μs	Error_rms@ 10 cm	0.0085	0.0019
0 - 0.25 μs	Error_pp@ 5 cm	0.1679	0.0114
0 - 0.25 μs	Error_rms@ 5 cm	0.0257	0.0036
0 – 1.3 μs	Error_pp@10 cm	4.1799	0.0062
0 – 1.3 μs	Error_rms@ 10 cm	3.0293	0.0017
0 – 1.3 μs	Error_pp@ 5 cm	3.8505	0.0147
0 – 1.3 μs	Error_rms@ 5 cm	2.8656	0.0032

In contrast, the proposed approach eliminates this accuracy limitation, providing well-matched results and enabling real-time tracking. Table III summarizes the quantitative error analysis. During the first quarter of the sinusoidal chirp (from 0-0.25 μs), where chirp ambiguity is absent, both methods show relatively low errors. For the proposed method, the peak-to-peak error (error_pp) is 0.0062 and 0.0114 for delay lengths of 10 cm and 5 cm, respectively - over ten times better than the Hilbert transform-based method. The calculated root mean square (error_rms) error further confirms the superior accuracy of the proposed DCD OPFD-based approach (0.0019 and 0.0036) compared to the Hilbert transform-based method (0.0085 and 0.0257), with 4-7 times better. When considering the ±chirp ambiguity region, error_pp and error_rms of the Hilbert transform-based method increase to 4.1799/3.8505 and 3.0293/2.8656 for 10 cm and 5 cm delay lines, respectively, while our proposed method still maintains consistent performance.

By adopting a simpler processing strategy, the overall computation time can be reduced. In MATLAB, we compare the proposed sample-by-sample method with the Hilbert Transform-based approach using the same number of samples (82801). The calculations are unwrap{angle[$S_1(t) + S_2(t) \times \mathrm{e}^{\frac{j2\pi}{3}} + S_3(t) \times \mathrm{e}^{\frac{j4\pi}{3}}$]} for the proposed method, and unwrap{angle[hilbert($S_1'(t)$)} for the Hilbert-based method, where angle() denotes the angle extraction and unwrap() denotes the phase unwrapping. The proposed approach takes 0.00857 seconds, which is merely 8.13% of the computation time of the Hilbert Transform-based method (0.105406 seconds). More importantly, the sample-by-sample processing enables true parallelism between data acquisition and data processing. In the traditional method, the processer must wait until all samples are collected before performing any calculation. In contrast, our approach allows ADCs to continue data sampling while the previous set of samples are being processed and then sent to DAC for output control. When the ADC/DAC sampling rate is much lower than signal processing speed, the effective system delay is essentially the ADC sampling interval. In the traditional way, however, the delay can be sounds of times longer, and increasing the processer speed does not alleviate this bottleneck.

In addition, the detective accuracy of the proposed scheme is also influenced by other factors such as the performance of the optical Hybrid and the performance of PDs. In real implementations, the optical Hybrid introduces both phase and amplitude errors. Specifically, the phase difference between its three outputs may deviate from the ideal 120° and their intensities may not be equal due to these imperfections. The hardware-caused imperfections are generally stable and can be compensated through DSP. The phase error can be measured and mitigated by replacing the phase set of [0, $2\pi/3$, $4\pi/3$] with the measured values in (18). Similarly, the intensity imbalance among three outputs can be combined with the PD responsivity imbalance and the electrical transmission line mismatch, requiring a unified compensation approach in DSP. As to the testing speed, in principle, the proposed approach could detect very high-speed frequency chirps (e.g., GHz level) by using a shorter time delay (it should be much faster than the frequency change) and upgrading the detection bandwidth such as using ultra-high-speed PDs and ADCs. For most practical applications such as optical spectral analysis and FMCW LiDAR, the chirp speed is approximately tens of MHz level and below, the low-speed devices (e.g., PDs and ADCs) could achieve good performance. When applying to high-speed applications, the cost of PDs, ADCs, and DSP increase significantly. The main technical limitation is that current solution requires another calibration module to get absolute wavelengths/frequencies.

IV. Applications

A. Laser Nonlinearity Correction in FMCW LiDAR

Currently, 3D sensors like LiDAR are proving to be effective for estimating targets at extended distances (∼200 m) [25]. Generally, there are two main LiDAR technologies: Time-of-Flight (ToF) and FMCW. ToF LiDAR suffers from more ambient interference and electrical noises than the FMCW approach (FMCW LiDAR). Another advantage of FMCW LiDAR over the ToF approach is its inherent velocity detection, significantly boosting object recognition capabilities [2]. However, the optical source generation in FMCW LiDAR is substantially more complex than that in ToF LiDAR. A FMCW LiDAR system generates a linear frequency chirp, and its frequency nonlinearity and phase noise will reduce the final performance of the FMCW LiDAR sensor. The realization of an FMCW optical generation module with high frequency chirp linearity and low phase noise in miniaturized and inexpensive manners is crucial. With this module, FMCW LiDAR will be a suitable technology for mass production, benefiting from its remarkable features.

There is an extensive prior art with respect to the linearization of FMCW LiDAR systems employing direct laser modulation [8], [23], [26], [27], [28]. This prior art focused on solving the linearization problem by applying advanced iterative algorithms. All the proposed linearization algorithms above utilize the phase of the resulting beat signal by applying the Hilbert transform.

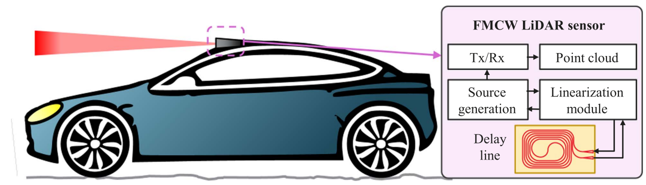

Fig. 9. Overview scheme of the linearization role in FMCW LiDAR sensors for automotive applications.

However, phase extraction based on Hilbert transform lacks accuracy, especially when the beat frequency is close to DC, as analyzed above. The detailed chirp linearization analysis is shown below. In a typical FMCW LiDAR system, the laser frequency sweep can be expressed with the following equation [8]:

$$\nu\left(t\right) = \nu_0 + \gamma t + \nu_{nl}\left(t\right) + \nu_{pn}\left(t\right), \tag{24}$$

where ν_0 is the starting optical carrier frequency in Hz and γ is the linear frequency swept slope in Hz^2. $\nu_{nl}(t)$ and $\nu_{pn}(t)$ are non-ideal terms, which represent the nonlinear part of the frequency swept and the instantaneous frequency induced by the phase noise, respectively. Ideally, $\nu_{nl}(t)$ and $\nu_{pn}(t)$ are null terms and, thus, the FMCW optical signal would be linear chirp. Nonetheless, laser realizations and environmental changes originate that the terms $\nu_{nl}(t)$ and $\nu_{pn}(t)$ are not null. More concretely, $\nu_{pn}(t)$ rapidly fluctuates with respect to chirp lengths in automotive FMCW LiDAR sensors. Thereby, $\nu_{pn}(t)$ or the laser phase noise requires to be constantly compensated in every chirp length slot [29]. On the other hand, the nonlinear component $\nu_{nl}(t)$ slowly changes with respect to $\nu_{pn}(t)$ and needs to be compensated less periodic. The compensation of the $\nu_{nl}(t)$ is commonly named as frequency linearization in the context of FMCW LiDAR. In addition, automotive scenarios are highly changing in terms of temperature fluctuation and mechanical vibration, which lead to the need of more periodical laser linearization procedure.

Fig. 9 represents the functionality of the laser linearization module within the FMCW LiDAR sensor in an autonomous vehicle. In Fig. 9, the linearization module is attached to the FMCW LiDAR engine which is made up of the source generation together with the transceiver. For chip integration, the FMCW LiDAR engine and the linearization block can be manufactured on the same chip (e.g., IMEC iSiPP200 platform in Section II). In the literature, a delay line is necessary for the laser linearization. This delay line is the optical component with biggest footprint in the linearization block and significantly contributes to the overall size of the PIC in the complete FMCW LiDAR sensor. Thus, the miniaturization of this delay line plays a crucial role for minimizing the PIC size of FMCW LiDAR sensors. The linearization process in the literature aims to obtain the intensity-frequency curve of the FMCW laser source $H(I(t))$. This intensity-frequency curve is estimated by using the beat-frequency resulting of an auxiliary MZI as an input of the linearization process. The beat-frequency signal of the linearization process can be modelled with the next formula [23]:

$$f_b\left(t\right) = \nu\left(t\right) + \nu\left(t - \tau_{ref}\right), \tag{25}$$

where τ_{ref} is the delay corresponding to the delay line in Fig. 9. In real applications, the laser linearization process is not ideal, remaining a residual value of $\nu_{nl}(t)$ in (24). There are two drawbacks originated by this residual $\nu_{nl}(t)$ in the FMCW LiDAR performance: range resolution deterioration and signal-to-noise ratio (SNR) reduction. The range resolution can be quantified with the following equation [8]:

$$\Delta D = \frac{c\,(1 + 2\pi \cdot \tau_{tar} \cdot \nu_{nl,rms})}{2 f_{exc}}, \tag{26}$$

where $\nu_{nl,rms}$ corresponds the RMS of $\nu_{nl}(t)$, τ_{tar} refers to the two-way target delay in second, and c is the speed of the light in the vacuum in m/s. f_{exc} is the entire excursion frequency chirp span. In parallel, the SNR reduction due to the residual $\nu_{nl}(t)$ term can be approximated as follows:

$$SNR_{out} \approx SNR_{in} \cdot \frac{\mathrm{erf}\left(2\sqrt{ln2}\right)}{1 + 2\pi \cdot \tau_{tar} \cdot \nu_{nl,rms}}, \tag{27}$$

where erf () indicates the Gaussian error function. In (27), it is assumed that the spectrum broadening due to the residual ν_{nl} of the beat signal follows a Gaussian shape, the fast Fourier transform (FFT) bin size is equal to $\Delta D_{ideal} = \frac{C}{2 f_{exc}}$, and the main noise contributor is additive (e.g., shot noise). Observing (26) and (27), it is relevant to mention that range resolution degradation and SNR reduction are proportional to the target distance. In other words, the side effects of the linearity inaccuracy are more severe for further away targets. Moreover, in the literature, the most used figure of merit to determine the quality of the linearization process is expressed as follows [8]:

$$1 - r^2 = 12 \cdot \left(\frac{\nu_{nl,rms}}{f_{exc}}\right)^2, \tag{28}$$

In Fig. 10, the drawbacks due to the nonlinearity term in the generated FMCW signal are quantified for different target distances and $1 - r^2$ values, where f_{exc} is set to 9 GHz. The graphs Fig. 10(a) and (b) are obtained by using (26) and (27), respectively. Inspecting Fig. 10(a) and (b), it can be observed the relation between the target distance and the drawbacks of the residual ν_{nl}, being more critical for further distances. Furthermore, the automotive requirement of the 5-cm range resolution is depicted in Fig. 10(a) [30]. The value of $1 - r^2$ below 1×10^{-7} is needed to meet the automotive requirement when the maximum detectable distance is 100 m. This $1 - r^2$ value goal signifies a maximum SNR reduction of approximately 3 dB for a target distance of 100 m (see Fig. 10).

Fig. 11(a) shows the chirp linearization of a laser based on the proposed angle-diversity structure for FMCW LiDAR sensors. A fiber-based architecture is designed for a proof-of-concept experiment. A triangular chirp signal is generated by an AWG (AFG3252) and then is fed into a laser driver (Koheron CTL200). Its output modulates the gain section of a distributed feedback (DFB) laser (DFB1550P) to periodically tune laser frequency. The wavelength is in the 1550 nm region. The repetition rate is set as 2 kHz with a 3-GHz tuning range. The laser output is then split into two parts. 90% of the light is used for LiDAR. 10% of the light is then fed into a fiber-based asymmetric

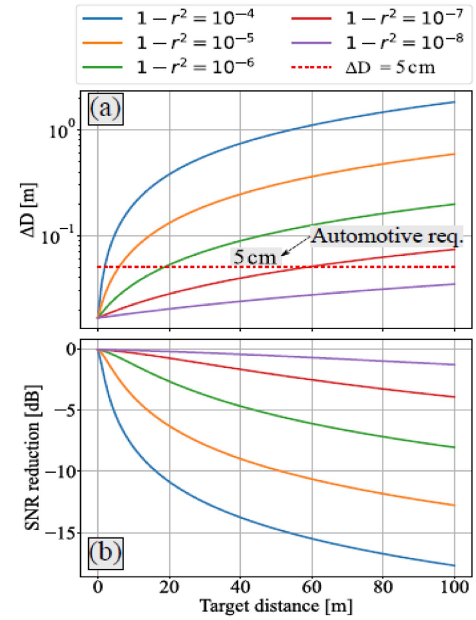

Fig. 10. Representation of the two drawbacks effect when laser linearization has residual error: range resolution degradation and SNR reduction as functions of the target distance for different values of $1-r^2$. Note: the selected excursion frequency of the laser is 9 GHz; the automotive requirement with respect to the range resolution is also illustrated with dotted red lines.

MZI where the lower arm has a longer delay line (0.25 m or 0.5 m or 2 m) with respect to the upper one. Two 50%:50% optical fiber couplers are used as the splitter and the combiner, respectively. The following block is the receiver with 4-angle diversity detection. As discussed in Section II, this receiver can be implemented in different manners. Considering that the 3-angle diversity structure is validated in the simulation part, this section investigates the 4-angle diversity approach. The receiver converts the input optical signal into four electrical beat signals with 90° phase shifting between adjacent channels via a free-space optics-based 90° optical hybrid (Exail COH090). Then two balance PDs (Thorlabs PDB570C) are used to convert optical signal into electrical signals. In the analog domain, signals at 0° and 180° phases are combined using a subtractor. This technique is often employed to cancel out common mode noise, as the subtractor effectively removes any identical components present in both signals. Similarly, signals at 90° and 270° phases can be considered equivalent in certain contexts. Each electrical signal passes through an individual block chain made of the following components: a TIA, a low-pass filter (LPF), and an ADC (a channel from a real-time oscilloscope). Finally, all the digitized signals from the ADCs are processed following the DSP block diagram represented in Fig. 11(b).

This DSP block diagram is utilized for laser linearization in an iterative manner. First, the iteration index i is set to zero. Then, a linear current $I_0(t)$ is applied to the laser by using an AWG. However, as indicated in [31], $I_0(t)$ can be set to the inverse function of $I(H)$ where H is the intensity-frequency curve of the used laser. In this manner, the linearization algorithm requires less iterations for converging to the same residual error ν_{nl}. Next, the ADC digitized signals from several chirp frames

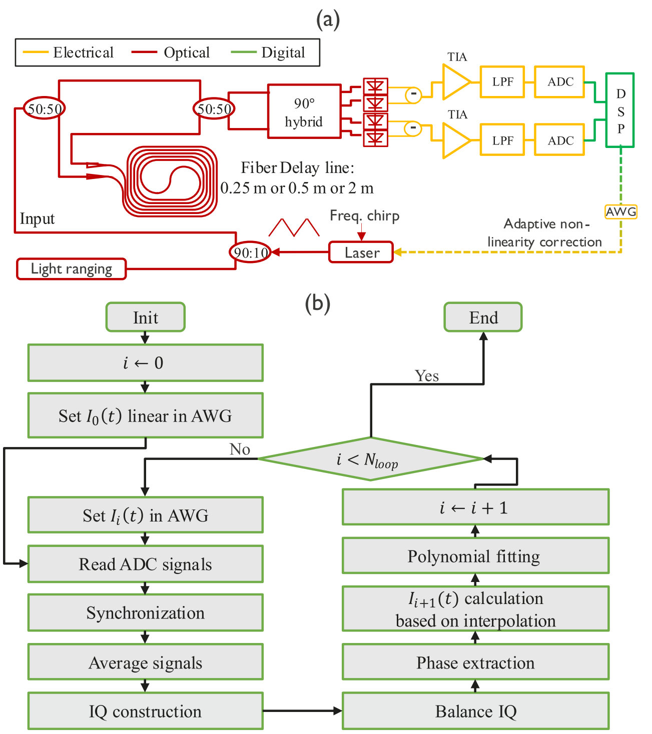

Fig. 11. (a) Experimental setup; (b) The signal processing algorithm of the chirp linearization in FMCW LiDAR.

are captured, synchronized, averaged to reduce additive noise disturbances in the linearization process. Then, IQ construction is performed. The IQ reconstruction uses the following formula:

$$S_{IQ}[n] = S_1[n] + j \cdot S_2[n], \tag{29}$$

$S_1[n]$ and $S_2[n]$are the ADC outputs (see Fig. 11(a)). When using the single balanced PD receiver, Hilbert transform is applied to extract the 90° equivalent from the unique ADC signal$S_1[n]$. Additionally, the Hilbert transform-based instantaneous frequency estimation lacks in accuracy, particularly at the edges, which limited the utilizable region of interest (ROI) and reduces the effective chirp length [8]. A shorter effective chirp length directly minimizes the final SNR of the system and, subsequently, the maximum detectable target distance. This method of constructing the IQ signal enables better linearization convergence rapidness and accuracy, since the phase estimation process is more reliable. The phase extraction block is executed by sequentially applying angle() and unwrap() functions. Subsequentially, a polynomial model is used to smooth the extracted phase, like [23]. The laser driving current $I_{i+1}(t)$ is then calculated by using the smoothed extracted phase, the actual current $I_i(t)$, and the interpolation process outlined in [27]. Finally, the iteration index i is updated and the iteration loop concludes when N loops are completed. Alternatively, the loop can end when a target accuracy better than the set $1-r^2$ value is achieved. Then, the loop ends when an accuracy meets the requirement using 100% of the ramp region (both up and down rump) with a fixed 2-m delay fiber. The frequency error is the difference between the calculated frequency and the desired frequency. And the calculated frequency is obtained from the phase item of the recovered complex signal. Here, we define the absolute amplitude fluctuation of the complex signal as the "Absolute Error", which reflects the IQ imbalance present in the recovered complex signal. This absolute error directly influences the phase error extraction, which in return contributes to the fluctuations in the frequency error in these graphs. As shown in Fig. 12(a), the Hilbert–transform–based method exhibits large frequency–error jumps at the edges of the ramps, accompanied by significant absolute–error fluctuations. Outside these edge regions, the frequency error becomes stable, with much smaller absolute–error variations. This behaviour results from inconsistencies in the Hilbert transform at the beginning and end of the generated 90–degree equivalent signal. Although the edge regions continue to show large frequency errors over several iterations, but the frequency error in the central portion of the ramps (approximately 95% of the ramp duration) is reduced, as illustrated in Fig. 12(b) for the case of $L_{ref} = 2$ m. In contrast, the proposed DCD–OPFD approach delivers superior performance, achieving frequency errors within ±2 MHz across the entire ramp after three iterations, enabled by more accurate frequency estimation.

The linearization performance is evaluated and compared between these two methods over different lengths of delay lines. To avoid the large frequency errors at the edges of the rumps, the parameter of $1 - r^2$ is calculated using 95% of the up and down rumps as presented in Fig. 12(b) [8]. And the large bias frequency errors in 95% of the rumps are also removed in this $1 - r^2$ calculation (marked as "removed offset" in Fig. 12(b)). When sufficient time delay (corresponding to a 2-m fiber) was used, the traditional method performs slightly worse than the DCD OPFD approach. However, the performance gap widens significantly as the delay line decreases from 2 m to 0.5 m and then 0.25 m (75% reduced), due to the decreased estimation accuracy of the LIF. These results prove simulation results in Fig. 8(a) and (b).

B. Laser Phase Noise Compensation

In this section, we introduce another important application for laser phase noise compensation (PNC). In our previous work [32], the laser phase/frequency noise is compensated by using the same 4-angle diversity structure. As analyzed in (12), a longer delay fiber (4 m) is employed to increase detection sensitivity. Although an increased time delay can reduce the accuracy of the OPFD model, the approximate 0.175 µs delay introduced by a 4-m fiber still ensures very high accuracy. In this proof-of-concept experiment, like the experimental setup in Fig. 13(a), both the frequency branch and the LiDAR branch are implemented. The employed FMCW source consists of a Thorlabs DFB laser (DFB1550P). The DFB laser is modulated with a pre-distorted ramp, calculated through a linearization process used in Section A. This pre-distorted ramp is generated utilizing the Tektronix AWG (AFG3252), with a sampling rate of 2 GSa/s. The CTL200 B-600 board from Koheron is employed as the laser driver, which injects a constant current of 650 mA to achieve an optical power of 100 mW at the laser output. Moreover, the excursion frequency of the laser is set to

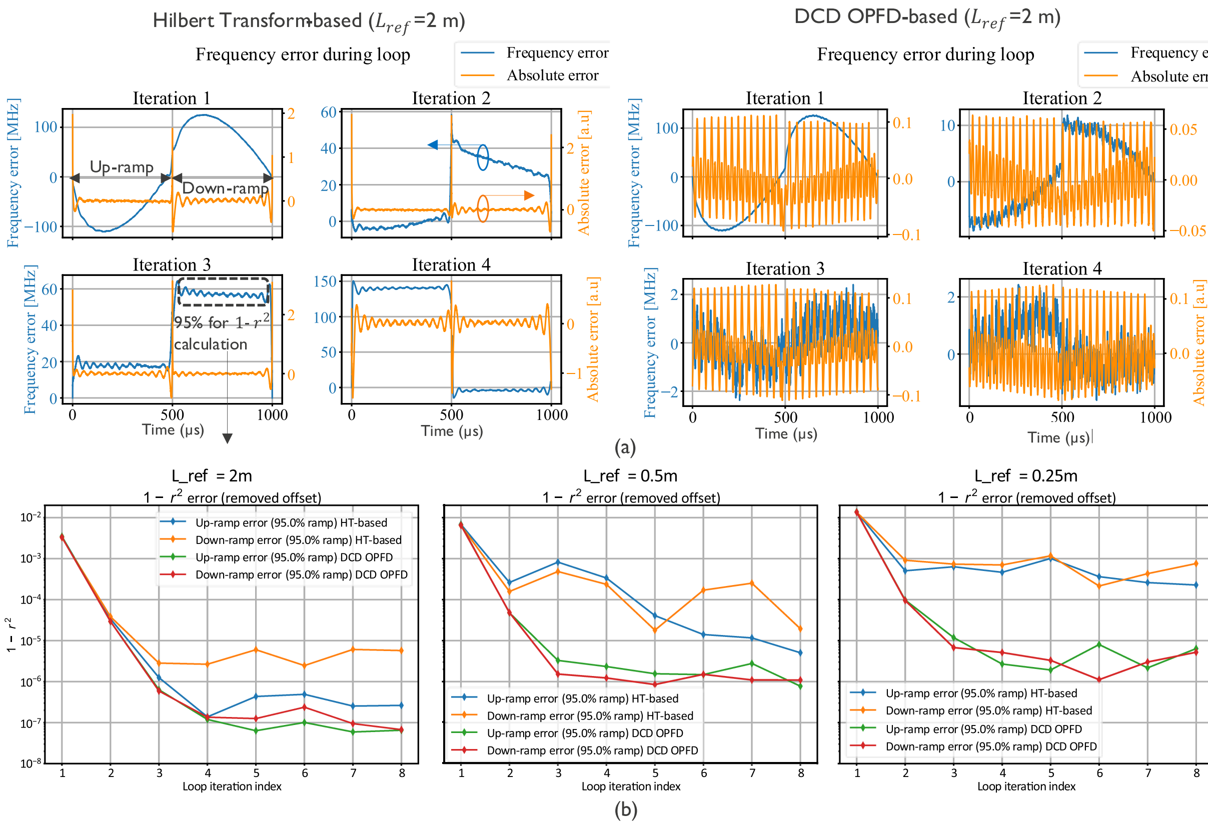

Fig. 12. (a) Frequency and absolute errors using 100% of the ramps; (b) the evaluation of the chirp nonlinearity using 95% of the ramps.

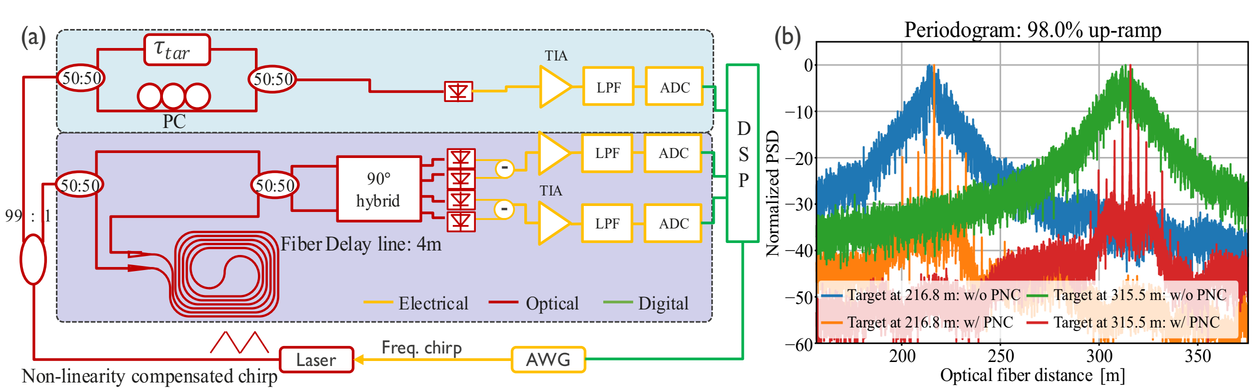

Fig. 13. (a) Experimental setup; (b) results of the phase noise compensation in FMCW LiDAR.

3 GHz, with an up-down chirp period is 1000 μs. After FMCW generation, the optical signal is split into two paths: one (99% of the light) for long-distance target emulation utilizing different optical patch cord lengths, and the other (1% of the light) for phase noise extraction assisted by an optical delay line of 4 m. More details can be found in [32]. In our experiment as shown in Fig. 13(b), the linewidth of the beat signal is significantly reduced by ∼1000 times to a 5.3-KHz level [32] utilizing 98% of the up-ramp signal. We evaluate sensing distances of 108.4 m and 157.75 m using fiber delay lines (216.8 m and 315.5 m) and observe similarly substantial performance improvements at both distances. Of course, the requirement for model accuracy varies with different frequency chirping speeds for different applications. The tradeoff between model accuracy and signal sensitivity needs to be taken into consideration when applying it to a new application.

C. Real-Time applications: Laser Wavelength Locker

Another significant advantage of the proposed technique is the ability to provide fast real-time responses. In this section, we present an example of its application in real-time photoelectric control loops to stabilize laser wavelength with ultra-high accuracy. Fig. 14(a) depicts the experimental setup. A laser wavelength locker (WLL) is commonly used in an optical transceiver for dense wavelength division multiplexing

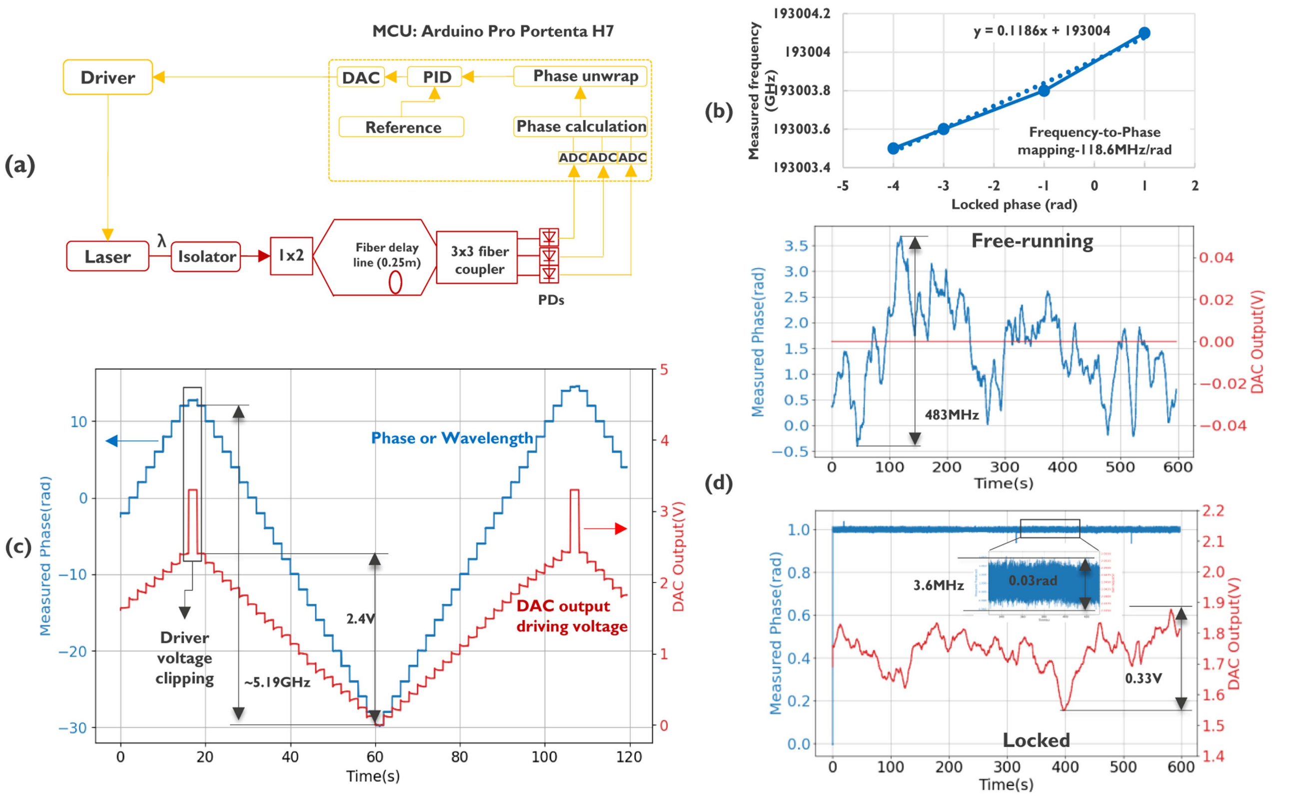

Fig. 14. (a) Experimental setup of the proposed WLL system; (b) the measured frequency-to-phase conversion factor; (c) step wavelength locking procedure; (d) laser stability evaluation before and after wavelength locking.

(DWDM) telecom/datacom applications, requiring frequency stability is below several gigahertz (e.g., $<\pm 10$ pm) [33]. Fig. 14 describes a low-cost micro controlling unit (MCU)-based WLL. A DFB laser from Thorlabs (DFB1550P) at 1550 nm is used to investigate the performance of the real-time control loop. An optical fiber isolator is used to eliminate the influence of reflections. One part of the light is then split through a 1-by-2 MMI, and its outputs are sent to our proposed 3-angle diversity laser frequency testing structure, which includes a 3x3 fiber coupler-based 120° optical hybrid, a fiber delay line of 0.25 m, and three PDs. An MCU (Arduino Pro Portenta H7) with embedded three ADCs and one DAC serve as the controlling and signal processing unit of the feedback loop. Inside the MCU, three signals are first sampled and used to recover the IQ signal, which is then used for phase extraction and unwrapping. The recovered laser frequency information is fed into a proportional–integral–derivative (PID) controller. The feedback signal is obtained by comparing it to a reference signal (e.g., a DC component). Finally, the new feedback signal is converted into the analog domain via an ADC. By real-time correcting the driving voltage of the laser's gain section, a WLL can actively stabilize the DFB laser.

More importantly, the locked frequency can be easily tuned by changing the reference value in digital domain. In principle, the laser can be continuously tuned to any wavelength. Before evaluating the WLL locking range and accuracy, the relationship between the measured phase and laser frequency was characterized, as shown in Fig. 14(b). The laser was locked to four reference values: -4, -3, -1, and 1. For each locking state, the central frequency was measured using a Finisar Wave Analyzer with a resolution of 150 MHz. The corresponding frequencies were 193.0035 THz, 193.0036 THz, 193.0038 THz, and 193.0041 THz, respectively. A linear fit of these data points yielded a phase-to-frequency conversion factor of 118.6 MHz/rad. Fig. 14(c) describes a step wavelength locking procedure. The total tuning range is $\sim$5.19 GHz. When the driving voltage is above 2.5 V, the voltage will be clipped, thus the laser will not be locked with any $>$2.5 V driving voltage. The selected locking reference value is from -30 radian to 14 radian with an increment of 2 radians. Fig. 14(d) shows the performance of the wavelength stabilization before and after locking. Laser frequency drifts $\sim$483 MHz over 10 minutes, while the laser is stabilized accurately after wavelength locking. The calculated laser frequency stabilizing accuracy is approximately 3.6 MHz (peak-to-peak phase value is 0.03 radians).

V. Conclusion

In this paper, we first introduce the real-time optical instantaneous frequency estimation approach with higher estimation accuracy than traditional Hilbert transform-based method. The proposed method utilizes an angle-diversity optical delayed self-heterodyne structure for direct complex-domain digital signal processing DSP. This approach eliminates $\pm$chirp ambiguity and significantly reduces errors in low-beat-frequency scenarios. By enabling shorter delay lines, it facilitates more compact on-chip integration and simplifies algorithm complexity, thereby minimizing DSP-induced delays. The sample-by-sample instantaneous frequency tracking supports real-time applications, such as fast feedback control loops. Additionally, the method can be working well in FMCW LiDAR nonlinearity corrections, FMCW LiDAR phase noise compensation, and real-time WLL with good achievements. Future work will address the key challenge of combining absolute wavelength/frequency calibration and our approach by incorporating either 1) an off–chip grating–based wavelength–meter technique [34] or 2) an on–chip optical–filter–based wavelength–meter design [35], [36], enabling broader application support.

References

[1] P. Del'Haye, O. Arcizet, M. L. Gorodetsky, R. Holzwarth, and T. J. Kippenberg, "Frequency comb assisted diode laser spectroscopy for measurement of microcavity dispersion," *Nature Photon.*, vol. 3, no. 9, pp. 529–533, 2009.

[2] A. Martin et al., "Photonic integrated circuit-based FMCW coherent LiDAR," *J. Lightw. Technol.*, vol. 36, no. 19, pp. 4640–4645, Oct. 2018.

[3] B. Behroozpour, P. A. M. Sandborn, M. C. Wu, and B. E. Boser, "Lidar system architectures and circuits," *IEEE Commun. Mag.*, vol. 55, no. 10, pp. 135–142, Oct. 2017.

[4] J. M. Schmitt, "Optical coherence tomography (OCT): A review," *IEEE J. Sel. Topics Quantum Electron.*, vol. 5, no. 4, pp. 1205–1215, Jul./Aug. 1999.

[5] W. Drexler and J. G. Fujimoto, *Optical Coherence Tomography: Technology and Applications*. Berlin, Germany: Springer, 2008.

[6] P. Shi et al., "Optical FMCW signal generation using a silicon dual-parallel Mach-Zehnder modulator," *IEEE Photon. Technol. Lett.*, vol. 33, no. 6, pp. 301–304, Mar. 2021.

[7] Y. Jiang et al., "Frequency modulation nonlinear correction and ranging in FMCW LiDAR," *IEEE J. Quantum Electron.*, vol. 60, no. 6, Dec. 2024, Art. no. 1400107.

[8] X. Zhang, J. Pouls, and M. C. Wu, "Laser frequency sweep linearization by iterative learning pre-distortion for FMCW LiDAR," *Opt. Exp.*, vol. 27, no. 7, pp. 9965–9974, 2019.

[9] P. Li, Y. Zhang, and J. Yao, "Rapid linear frequency swept frequency-modulated continuous wave laser source using iterative pre-distortion algorithm," *Remote Sens.*, vol. 14, no. 14, 2022, Art. no. 3455.

[10] E. Ip, A. P. T. Lau, D. J. Barros, and J. M. Kahn, "Coherent detection in optical fiber systems," *Opt. Exp.*, vol. 16, no. 2, pp. 753–791, 2008.

[11] K. Sayyah et al., "Fully integrated FMCW LiDAR optical engine on a single silicon chip," *J. Lightw. Technol.*, vol. 40, no. 9, pp. 2763–2772, May 2022.

[12] 2025. [Online]. Available: https://en.wikipedia.org/wiki/Hilbert_transform

[13] T. J. Ahn and D. Y. Kim, "Analysis of nonlinear frequency sweep in high-speed tunable laser sources using a self-homodyne measurement and Hilbert transformation," *Appl. Opt.*, vol. 46, no. 13, pp. 2394–2400, 2007.

[14] X. Zhang et al., "Highly-accurate real-time instantaneous frequency estimation of a fast-chirped laser and its application for FMCW LiDAR nonlinearity correction," in *Proc. Opt. Fiber Commun. Conf. Exhib.*, 2025, pp. 1–3.

[15] J. Parker, J. Bauters, J. E. Roth, E. Norberg, and G. A. Fish, "Integrated wavelength locker," U.S. Patent EP3306836A1, Apr. 29, 2020.

[16] X. S. Yao et al., "On-chip real-time detection of optical frequency variations with ultrahigh resolution using the sine-cosine encoder approach," *Nature Commun.*, vol. 16, 2025, Art. no. 3092.

[17] Z. Li, L. Zhou, L. Lu, S. Zhao, D. Li, and J. Chen, "4×4 nonblocking optical switch fabric based on cascaded multimode interferometers," *Photon. Res.*, vol. 4, no. 1, pp. 21–26, 2016.

[18] S. H. Jeong and K. Morito, "Novel optical 90° hybrid consisting of a paired interference based 2x4 MMI coupler, a phase shifter and a 2x2 MMI coupler," *J. Lightw. Technol.*, vol. 28, no. 9, pp. 1323–1331, May 2010.

[19] 2025. [Online]. Available: https://en.wikipedia.org/wiki/Euler%27s_formula

[20] S. Y. Siew et al., "Review of silicon photonics technology and platform development," *J. Lightw. Technol.*, vol. 39, no. 13, pp. 4374–4389, Jul. 2021.

[21] J. Lambrecht et al., "90-Gb/s NRZ optical receiver in silicon using a fully differential transimpedance amplifier," *J. Lightw. Technol.*, vol. 37, no. 9, pp. 1964–1973, May 2019.

[22] Y. Yu, J. Guo, K. Tian, K. Liu, Z. Wang, and Z. Liu, "High-resolution optical frequency rapid measurement method based on the hilbert transform for extracting instantaneous frequency," *IEEE Sensors J.*, vol. 24, no. 24, pp. 41695–41701, Dec. 2024.

[23] J. Yang et al., "High-ranging-precision FMCW LiDAR with adaptive pre-distortion of current injection to a semiconductor laser," *J. Lightw. Technol.*, vol. 42, no. 6, pp. 1870–1876, Mar. 2024.

[24] F. J. Ferraro et al., "Imec silicon photonics platforms: Performance overview and roadmap," *Proc. SPIE*, vol. 12429, Mar. 2023, Art. no. 1242909.

[25] J. Liu, Q. Sun, Z. Fan, and Y. Jia, "TOF lidar development in autonomous vehicle," in *Proc. IEEE 3rd Optoelectron. Glob. Conf.*, 2018, pp. 185–190.

[26] H. Chen et al., "Interpolation linearization predistortion technology for FMCW LiDAR," *Appl. Opt.*, vol. 63, pp. 1538–1545, Feb. 2024.

[27] P. Li, Y. Zhang, and J. Yao, "Rapid linear frequency swept frequency-modulated continuouswave laser source using iterative pre-distortion algorithm," *Remote Sens.*, vol. 14, no. 14, Jul. 2022, Art. no. 3455.

[28] Y. Meng et al., "Dynamic range enhanced optical frequency domain reflectometry using dual-loop composite optical phase-locking," *IEEE Photon. J.*, vol. 13, no. 4, Aug. 2021, Art. no. 7100307.

[29] F. Ito, X. Fan, and Y. Koshikiya, "Long-range coherent OFDR with light source phase noise compensation," *J. Lightw. Technol.*, vol. 30, no. 8, pp. 1015–1024, Apr. 2012.

[30] H. Holzh¨uter, J. B¨odewadt, S. Bayesteh, A. Aschinger, and H. Blume, "Technical concepts of automotive LiDAR sensors: A review," *Opt. Eng.*, vol. 62, no. 3, Jan. 2023, Art. no. 031213.

[31] X. Cao, K. Wu, C. Li, G. Zhang, and J. Chen, "Highly efficient iteration algorithm for a linear frequency-sweep distributed feedback laser in frequency-modulated continuous wave lidar applications," *J. Opt. Soc. Amer. B*, vol. 38, no. 10, pp. D8–D14, Oct. 2021.

[32] J. P. Santacruz, J. Romme, X. Zhang, E. V. Araujo, M. Dahlem, and R. M. Oldenbeuving, "Analysis and compensation of phase noise in FMCW LiDAR sensors," *J. Lightw. Technol.*, vol. 43, no. 12, pp. 5636–5644, Jun. 2025.

[33] H. Nasu et al., "Wavelength monitor integrated CW DFB laser module for DWDM applications," Furukawa Elevtric Co., Ltd. Japan, Furukawa Review, vol. 23, 2003.

[34] 2025. [Online]. Available: https://www.optoplex.com/Wavelength_Locker.htm#:~:text=Temperature%20Sensor%20Supply%20Voltage,Tunable%20Comb%20Filter

[35] B. Stern, K. Kim, H. Gariah, and D. Bitauld, "Athermal silicon photonic wavemeter for broadband and high-accuracy wavelength measurements," *Opt. Exp.*, vol. 29, no. 19, pp. 29946–29959, 2021.